

JOINT HIGH TEMPERATURE OBSERVATION OF A SMALL C6.5 SOLAR FLARE WITH IRIS/EIS/AIA

POLITO V.

DAMTP, CMS, University of Cambridge, Wilberforce Road, Cambridge CB3 0WA, United Kingdom

REEVES, K.K.

Harvard-Smithsonian Center for Astrophysics, 60 Garden Street, Cambridge MA 01238, USA

DEL ZANNA, G.

DAMTP, CMS, University of Cambridge, Wilberforce Road, Cambridge CB3 0WA, United Kingdom

GOLUB, L.

Harvard-Smithsonian Center for Astrophysics, 60 Garden Street, Cambridge MA 01238, USA

MASON, H.E.

DAMTP, CMS, University of Cambridge, Wilberforce Road, Cambridge CB3 0WA, United Kingdom

Draft version March 18, 2015

ABSTRACT

We present the observation of a C6.5 class flare on 2014 February 3, obtained with the Interface Region Imaging Spectrograph (IRIS) and the EUV Imaging Spectrometer (EIS) on board HINODE. We follow the details of the impulsive phase with IRIS and the gradual decay phase with both IRIS and EIS. The IRIS Slit-Jaw Imager and Atmospheric Imaging Assembly (AIA) are used to precisely co-align the two sets of spectroscopic observations. Of particular interest is the Fe XXI 1354.08 Å spectral line, which is the highest temperature emission (~ 10 MK) observed in the IRIS wavelength range. We show the evolution of the Fe XXI profiles during the impulsive phase of the flare at the same ribbon location with a 75 s temporal cadence. Totally blue-shifted (~ 82 km s^{-1}) profiles are found at the very early phase of the flare and gradually decrease in about 6 minutes. This result is consistent with 1-D model predictions during chromospheric evaporation in flares. The blue shifted components also exhibit large non-thermal broadening, which decrease simultaneously with the blue-shifted velocity. After the evaporation first occurs, the Fe XXI intensity progressively moves from the footpoints to the top of the hot flare loops seen in the AIA 131 Å images, where the emission is observed to be at rest and thermal. Emission measure estimates from IRIS/EIS/AIA observations during the gradual phase show isothermal loop top structures cooling from about 13.5 MK to 12 MK with electron densities of the order $\sim 5 - 6 \cdot 10^{10} \text{ cm}^{-3}$.

Keywords: Sun: flares, Sun:UV spectra, techniques: diagnostics, Sun: chromospheric evaporation

1. INTRODUCTION

The current models proposed to explain processes involved in flares and flare-related events still lack completeness and include many unsolved questions. The standard model of flares (Carmichael 1964; Sturrock 1968; Hirayama 1974; Kopp & Pneuman 1976) represents a simple theoretical scenario which is commonly assumed when interpreting observational results. It suggests that the energy released from magnetic reconnection in the corona heats the local plasma or alternatively accelerates non-thermal particles towards the chromosphere, where they encounter a denser environment and are stopped by particle collisions. In both cases, the result is an intense heating of the chromospheric plasma to coronal temperature with consequent expansion and filling of coronal loops, through a process called “chromospheric evaporation”. Other models have been also proposed, which include alternative explanations to the transport of energy from the corona, such as large-scale Alfvén waves (Fletcher & Hudson 2008) or which suggest that the site

of energy release could be located to greater depths in the chromosphere (Brosius & Holman 2009; Brosius 2013b). A definitive model should be able to reproduce the wide range of observations from different space satellites over the past decades (Benz 2008; Fletcher et al. 2011). Spectral signatures of chromospheric evaporation are velocity blueshifts in the high temperature emission originating from flare kernels, which were first observed in the X-ray wavelength range by SOLFLEX (Doschek et al. 1979) and the Solar Maximum Mission (SMM) (Antonucci et al. 1982). These spectra (8-25 MK) showed turbulent velocities exceeding 100 km s^{-1} and blueshifted components (up to ~ 400 km s^{-1}) superimposed on a dominant at-rest plasma component. Blue wing asymmetries (upward velocity ~ 200 km/s) were also found in Fe XXI 1354.08 Å spectra ($T \gtrsim 10$ MK) with the SMM Ultraviolet Spectrometer and Polarimeter (Mason et al. 1986). Theoretical models of chromospheric evaporation in a single flare loop would predict the presence of a completely blueshifted component (Emslie & Alexan-

der 1987), in contrast to what was found in these early spectroscopic results. The discrepancy can be explained by interpreting these asymmetric profiles as the superposition of plasma components at different velocities in sub-resolution strands within the loop (Doschek & Warren 2005).

The advent of spatially resolved spectroscopy has however shown a very different picture of the chromospheric evaporation during the impulsive phase of flares. Some of the earlier observations were obtained with the Coronal Diagnostic Spectrometer (CDS; Harrison et al. (1995)) on board the Solar and Heliospheric Observatory (SOHO), which allowed measurements of chromospheric, transition-region and coronal lines, as well as the Fe XIX (9 MK) flare line. Del Zanna et al. (2006) presented a clear observation of a totally blueshifted (~ 140 km s^{-1}) and non-thermal broadened Fe XIX line profile during the impulsive phase of an M1 class flare on 2002 October 22. Other studies based on CDS observations found similar results (Brosius 2003; Milligan et al. 2006). These observations are in agreement with 1-D hydrodynamic modelling of the response of the plasma during chromospheric evaporation. Del Zanna et al. (2006) also showed that lines formed above 1 MK were progressively more blueshifted as their formation temperature increases, and small downflows in the cooler lines were also observed.

The launch of the EUV Imaging Spectrometer (EIS; Culhane et al. (2007)) on board the Hinode satellite significantly improved our knowledge of chromospheric evaporation and plasma dynamics. EIS provides a wide temperature coverage by observing emission lines typical of transition region (e.g., O V 192.90 Å, 248.46 Å formed at 0.2 MK, Young et al. (2007)) to flare temperatures (e.g., Fe XXIII 263.76 Å, Fe XXIV 192.03 Å and 255.11 Å, formed from 10 to 30 MK, Del Zanna et al. (2005)). Several papers based on EIS observations presented shifts in emission lines formed at different temperatures, substantially confirming the picture that emerged from SOHO CDS. In particular, Watanabe et al. (2010) presented evidence of “explosive” chromospheric evaporation in the rising phase of a C9.7 flare, a two component spectrum with a dominant upflowing emission of ~ 382 km s^{-1} is observed from one of the flare footpoints. Dominant blue-shifted components of the order of 400 km s^{-1} were also measured in Fe XXIII and Fe XXIV lines by Young et al. (2013).

Another instructive example is reported in Del Zanna et al. (2011a), where they observed slightly broadened and completely blue-shifted (~ 90 km s^{-1}) Fe XXIII profiles during the peak of a small B2 class flare. More recently, Brosius (2013a) presented a sit-and-stare study of a C1 class where they observed totally shifted Fe XXIII profiles by upflowing velocities up to about 206 km s^{-1} .

Temperature-dependent velocity measurements were also reported by Milligan & Dennis (2009) from EIS.

It is important to keep in mind that neither CDS nor EIS observed photospheric lines, hence the dopplershift measurements were done relative to regions of the quiet Sun (whenever observed) assuming that the line emission there was at rest. Another issue when analysing EIS spectra is the 70 km s^{-1} shift of the wavelength scale

during the orbital motion of the satellite Kamio et al. (2010), which introduces an additional uncertainty in the estimation of the rest wavelength (e.g., Kamio et al. 2010; Young et al. 2012, ~ 5 km s^{-1}). Finally, the blendings of the CDS and EIS flare lines and the limited number of points acquired across the spectra affected the measurements of line profiles and non-thermal broadenings.

Since July 2013, the Interface Region Imaging Spectrograph (IRIS, De Pontieu et al. (2014)) has been acquired simultaneous spectra and images of the solar atmosphere at very high temporal (up to 2s) and spatial (0.33”-0.4”) resolution. The IRIS Slit Jaw Imager (SJI) provides high-resolution images in four different passbands (C II 1330 Å, Si IV 1400 Å, Mg II k 2796 Å and Mg II wing 2830 Å). At the same time, the IRIS spectrograph (SP) observes continua and emission lines formed over a very broad range of temperatures, from $\log(T)[K] = 3.7 - 7$.

The highest temperature line ($\gtrsim 10$ MK) observed by IRIS is the Fe XXI spectral line at 1354.08 Å, which was first identified by Doschek et al. (1975) with the Naval Research Laboratory’s Spectroheliograph on board Skylab. The spatial and spectral characteristics of this line provide useful information for studying chromospheric evaporation during flares. Mason et al. (1986) observed blueshifted asymmetric Fe XXI profiles from the footpoints of the flare loops which indicated upflows in excess of 200 km s^{-1} during the impulsive phase of different flare events. In the same work, Fe XXI observations during the thermal phase showed line widths which were consistent with the expected thermal width.

The Fe XXI 1354.08 Å spectral line has also been observed with the Solar Ultraviolet Measurement of Emitted Radiation (SUMER) on board SOHO. To the best of our knowledge, SUMER has not reported any significant Fe XXI observation at the footpoints of flare loops during the impulsive phase. Finally, we would like to point out that none of the instruments mentioned above could reach the high spatial and temporal resolution capabilities of IRIS.

The IRIS observation of a X1 class flare in March 2014 has recently been reported by Young et al. (2014). In this event, Fe XXI blue shifts of the order ~ 100 km s^{-1} and up to 200 km s^{-1} are observed at different ribbon locations from the impulsive phase until ~ 6 minutes after the peak of the flare. In addition, Fe XXI profiles at the top of the flare arcade are at-rest and show widths close to the thermal width.

We are particularly interested in analysing joint observations of flares with both IRIS and Hinode/EIS. Combining observations from both instruments for the same event can provide us with a better understanding of the plasma dynamics. We performed a search over the first year of the IRIS mission to look for flares observed by both IRIS and EIS. We specifically searched for observations of small flares where the instruments were scanning over the same location and close in time. Small flares are preferred to avoid saturation and to fit within the field-of-view of IRIS and EIS. Only a few of such events were found.

In this work, we focus on studying chromospheric evaporation seen in the Fe XXI emission during the impulsive phase of a C6.5 flare observed by IRIS on 2014 February 3. We also compare our results with the EIS observations of the same event in high temperature lines (Fe XXIII, Fe XXIV) during the gradual phase of the flare. The Atmospheric Imaging Assembly (AIA; Lemen et al. 2012) on board the Solar Dynamics Observatory (SDO) and the IRIS Slit Jaw Imager provide context information in order to precisely co-align observations from the two spectrometers.

The paper is structured as follows. Sect. 2 presents the context of the AIA, IRIS and EIS observations. The evolution of the flare as observed by the three instruments is then described in detail in Sect. 3. Sect. 4 presents the analysis and spectroscopic results of the IRIS Fe XXI spectral line. In sect. 5 we calculate emission measures and densities at the loop top during the gradual phase. Finally, in Sect. 6 we discuss and summarize our work.

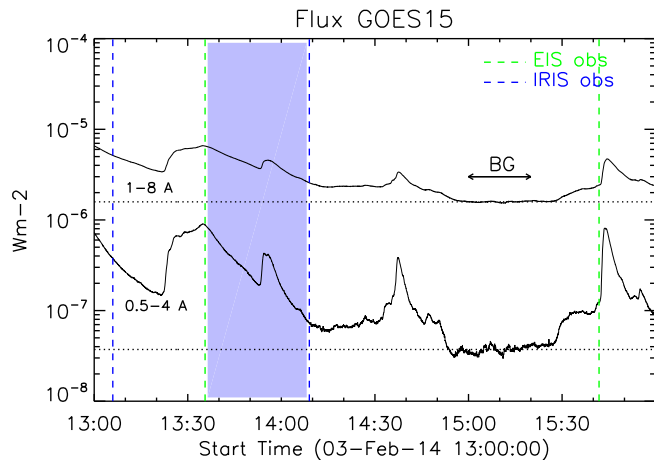


Figure 1. Light curves of the 3rd February 2014 flare in two GOES channels: 0.5-4 Å and 1-8 Å. The vertical coloured lines define the start and end of the IRIS (blue) and EIS (green) observations. The filled area shows the interval where the set of two observations overlap. The timing of the background emission is indicated by horizontal arrow BG.

2. CONTEXT OF THE OBSERVATIONS

The event under study is a C6.5 class flare which occurred on the 3rd February 2014 in the AR 11698. Figure 1 shows the GOES light curves of the event in the channels 1-8 Å and 0.5-4 Å. A C7.9 class flare occurred from 12:43 to 13:05 UT in a different location inside the same active region 11698 (see caption in fig. 2). Its declining emission is still visible in the GOES curves in fig.1 until around 13:20 UT. The C6.5 class flare started at about 13:21 UT, peaked at 13:34 UT and finished at about 13:44 UT. However, other post-flare peaks in the same region are visible in the GOES soft X-ray curves at about 13:54 UT and 14:36 UT (see sect.3). The green and blue vertical dotted lines show the start and the end of the EIS and IRIS observations, respectively. IRIS follows the whole evolution of the flare from 13:06 to 14:09 UT. The EIS observations cover only the gradual phase,

starting at about 13:35 UT and finishing at 15:41 UT. The blue shaded area denotes the interval where the set of two observations overlap. The horizontal arrow (BG) indicates a quiet interval that can be used to estimate the background soft X-ray emission (indicated by the horizontal dotted lines in fig.1).

Figure 2 shows SDO/AIA images of the flare in the 94 Å and 1600 Å channels. They were taken at around 13:37:50 UT, which is the closest time to the mid-point of the first EIS raster. The flare ribbons are best seen in the 1600 Å image, while the 94 Å images are dominated by plasma at $T \sim 7$ MK (Petkaki et al. 2012). The fields of view of EIS and IRIS are denoted by the yellow and pink boxes in fig. 2. In addition, the white box encloses the region over which the AIA light curves have been calculated (see Sect.2.1). The IRIS spectrograph scans from east to west, it mainly observes the northern ribbon and only a small part of the southern one. EIS scans both ribbons from west to east.

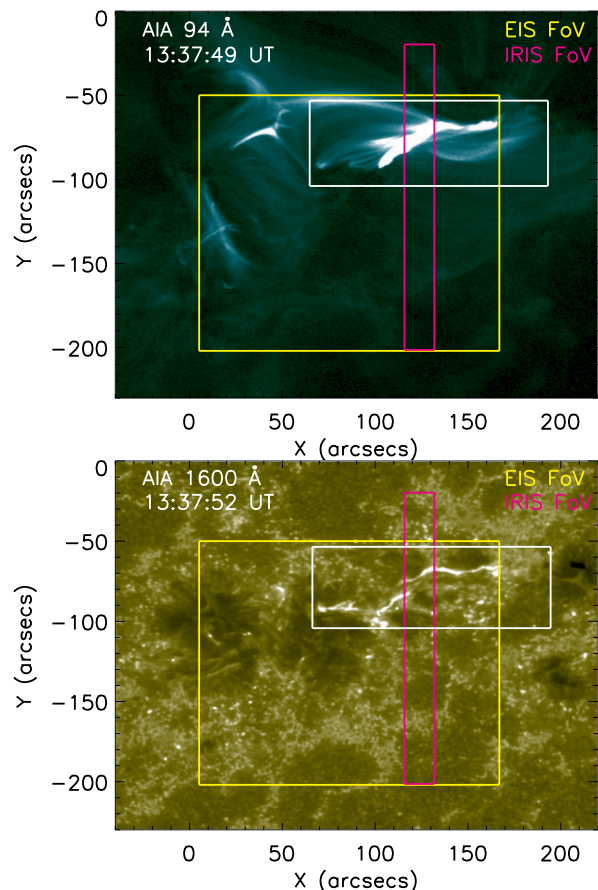


Figure 2. AIA 94 Å (top) and 1600 Å (bottom) images of the 3rd February 2014 flare taken about 3 minutes after the peak. IRIS (pink) and EIS (yellow) fields of view are overplotted. The white box defines the region where the AIA light curves have been calculated. The IRIS spectrograph scans from east to west while EIS scans from west to east. A C7.9 class flare peaked at about 12:54 UT in the same AR but in a different location, centred around the solar coordinates (-40, -80) arcseconds in the figure above.

The details of the observation are given in Sect.2.1 (SDO/AIA), Sect.2.2 (IRIS) and Sect.2.3 (EIS). The images from the three instruments were accurately co-

aligned as described in section 2.4.

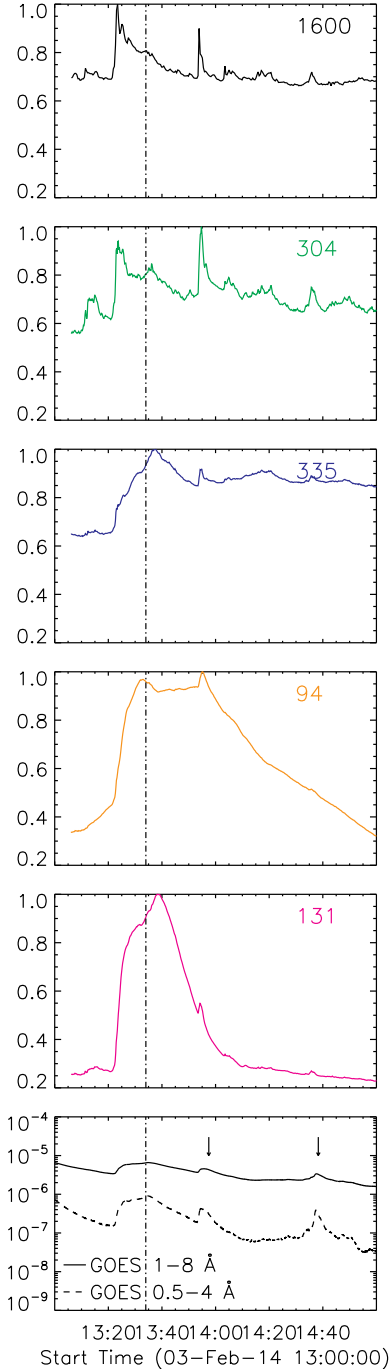


Figure 3. AIA light curves in 4 different EUV and one UV filters. For each filter, the emission has been averaged over the white box shown in figure 2. The dotted vertical line defines the peak of the flare in the soft X-ray emission. GOES light curves are also shown for comparison in the bottom panel. The small vertical arrows indicate the post-flare peaks also visible in the AIA images (fig. 4).

2.1. SDO AIA observation

The SDO/AIA level 1 data analyzed in the present work were downloaded through the cut out ser-

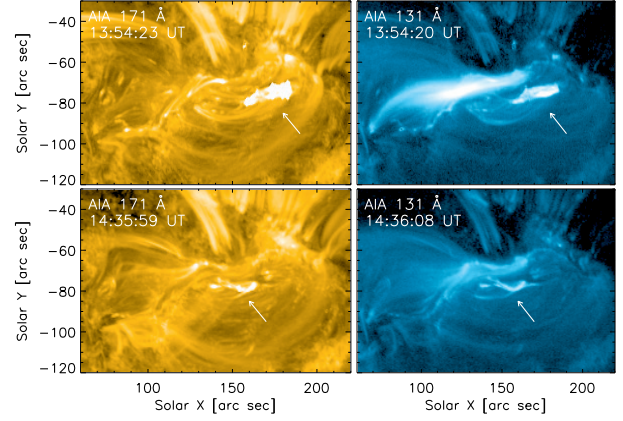


Figure 4. The post-flare brightenings in the AIA filters are associated with coronal loops between the ribbons (indicated by the small white arrows), which are visible in all the AIA filters.

Table 1
Study details of the joint IRIS EIS observation

Study details	EIS	IRIS SP
Start (UT)	13:35:35	13:06:21
End(UT)	15:43:18	14:09:19
Slit width	2"	0.33"
FoV	162" x 152"	14" x 174"
Exp.No.	54	8
Exp. cad.(s)	3	8
Raster No.	24	50
Raster cad.(s)	250	75

vice http://www.lmsal.com/get_aia_data/. They were mainly processed by using the IDL solarsoft routines available within the solarsoft distribution. The Point Spread Function (PSF) was deconvolved with the *aia_deconvolve_richardsonlucy.pro* solarsoft routine. Deconvolving the PSF can be useful in order to remove diffraction and scattering patterns created by the telescope optics. The AIA data were then converted to level 1.5 images by using the *aia_prep.pro* routine and finally corrected for solar rotation. Figure 3 shows the AIA light curves from 13:00 UT to 15:00 UT in 4 different EUV filters and one UV filter. The remaining three AIA EUV filters are not shown because they are badly (171 Å, 193 Å) or partially (211 Å) saturated during the flare. For each of the non-saturated filters, the emission has been averaged over the region enclosed by the white box in fig 2 and normalized to its maximum. The vertical dotted line in figure 3 defines the time of the peak of the flare in the soft X-rays (13:34 UT). The GOES light curves are also plotted at the bottom for comparison. The light curves in the cooler 1600 Å and 304 Å channels peak sharply at about 13:22 UT. The 1600 Å filter is mainly dominated by chromospheric emission, while the 304 Å filter includes emission from He II, formed at around 0.05 MK. The IRIS Slit Jaw images in the chromospheric 1330 Å and 1400 Å filters also brighten at about the same time than the AIA 1600 Å channel. As mentioned in sect.2, the GOES light curves (bottom

panel) show two post-flare peaks at around 13:54 UT and 14:36 UT, which are denoted by the vertical arrows in figure 3. At these times, different loops connecting the ribbons become visible in all the AIA filters. Figure 4 shows an example in the closest AIA 171 Å and 131 Å channels images with the position of the flaring loops indicated by white arrows. This suggests that smaller energetic events were still on going at those times.

2.2. IRIS observation

The IRIS level 2 data were retrieved from the instrument website <http://iris.lmsal.com/search>. Level 2 images represent the recommended product for scientific use. They are obtained from level 0 data after flat-field and geometry calibration and dark current subtraction. Cosmic rays have been then removed from level 2 data by using the solarsoft routine *despik.pro*. On 3rd February 2014 the IRIS spectrograph was running a sparse 8-steps raster observation from 13:06:21 to 14:09:19 UT. For each of the 50 rasters, the 0.33" slit was scanning from east to west over a $14 \times 174 \text{ arcsec}^2$ field of view in about 75 s. The IRIS field of view is denoted by the pink rectangular box in figure 2. Each slit position is separated by 2" and has an exposure time of 8 s, giving an actual step cadence of about 9.4 s. The observing study uses 9 narrow wavelength windows, most of which contains at least one or more spectral lines. The FUV detector covers 5 of the 9 windows (FUVS: C II 1336 Å, 1343 Å, Fe XII 1349 Å, O I 1356 Å; FUVL: Si IV 1402 Å) while the remaining 4 windows are observed by the NUV detector (2832 Å, 2826 Å, 2814 Å, Mg II k 2796 Å). The details of the observational sequence are given in table 1. In this work we only focus on the O I 1356 Å spectral window which contains the Fe XXI 1354.08 Å emission line. The IRIS Slit Jaw Imager obtained 19 s cadence images in the 1330 Å and 1400 Å filters of an area of $166 \times 174 \text{ arcsec}^2$ on the Sun. For each spectrograph exposure, one context SJI image is provided either in the 1330 Å or 1400 Å filter alternatively.

2.3. EIS observation

The EIS study HH_FLARE_162X152 was run from 13:35:35 UT to 15:43:18 UT on the 3rd of February 2014. It contains 24 sparse rasters covering an area on the Sun of $162 \times 152 \text{ arcsec}^2$ in 250 s. For each raster, the 2" slit scanned 54 positions with a 3 s exposure time, with a 1" jump between each position. In contrast to IRIS, EIS scans from west-to-east. This study includes 12 spectral windows. However, we have focused our analysis only on the high temperature Fe XXIII 263.76 Å and Fe XXIV 192.03 Å and 255.11 Å spectral lines. The details of the EIS observation are also given in table 1.

The EIS data have been reduced to level 1 with the Solarsoft IDL routine *eis_prep.pro*. We used standard options in order to remove hot and dusty pixels and interpolate missing pixels, as described in the EIS wiki notes¹. We have then applied the radiometric calibration method described in Del Zanna (2013) which corrects the EIS ground calibration for the degradation of the instrument efficiency over time. Warren et al. (2014) have also recently investigated the absolute EIS calibration, see sect. 5 for further discussion. The data have also

been corrected to account for the offset (about 18 pixels) in the solar-Y direction between the LW and SW CCD channels. When performing velocity measurements, it is also important to take into account the EIS wavelength scale drift with time due to orbital motion and the lack of an absolute wavelength calibration. In this study we are not interested in measuring doppler shifts in the EIS line profiles which are observed only during the gradual phase; the issues related to the wavelength calibration therefore do not represent a major problem.

2.4. Cross alignment between AIA, EIS and IRIS SJI images

IRIS and EIS were observing the same active region on the Sun, but their pointing coordinates can differ by few arcseconds. This is due to the pointing uncertainty of the two instruments (up to 10 arcseconds for EIS and ~ 5 arcseconds for IRIS). SDO/AIA and SJI images were used to precisely co-align the monochromatic images from EIS and IRIS. EIS Fe XVI 262.98 Å images can be aligned to AIA 335 Å maps, which are mainly dominated by Fe XVI emission, formed at about $T \sim 3$ MK. The IRIS SJI 1330 Å filter mainly includes emission from C II 1334/1335 Å formed at $T \sim 0.02$ MK. Those observation can thus be directly compared and aligned with AIA 1600 Å chromospheric images. Once the EIS and IRIS images are both aligned to co-temporal AIA images, we can then derive the relative co-alignment between the two spectrometers. All the images were cross-aligned by eye, giving an uncertainty of about 2 AIA pixels (~ 1.2 arcseconds), which is small compared to the IRIS and EIS field-of-view.

3. EVOLUTION OF THE FLARE

Figure 5 shows IRIS SJI 1330 Å (top) and the closest AIA 131 Å images (bottom) at different times during the evolution of the flare. In each of the SJI images, the pink contours denote the intensity of the Fe XXI emission line observed by the IRIS spectrograph. In the last two top images, the EIS Fe XXIII intensity contours are also overlaid (yellow). During flares, the AIA 131 Å channel is dominated by Fe XXI and therefore shows the evolution of the 10 MK flare plasma. Both AIA and IRIS SJI images are taken at the closest time to the mid-point of the IRIS and EIS rasters.

By overlapping high spectral resolution Fe XXI observations to context SJI images at lower temperatures, we can precisely define the ribbon locations where the Fe XXI intensity originates and follow its evolution over time. Co-temporal high cadence AIA 131 Å images also provide useful information to study the hot temperature plasma. The first SJI image on the left is taken while the IRIS spectrograph was scanning the raster no. 13 (13:22:43-13:23:49 UT) during the rising phase of the flare, as can be seen in the light curves in figure 3. In this raster the IRIS Fe XXI emission is visible for the first time. However, its intensity becomes stronger only during the following raster (no.14; 13:23:59-13:25:05 UT), which is shown in the second SJI image. The third image shows the morphology of the plasma about 4 minutes prior the peak of the flare. At this time, the Fe XXI intensity is

¹ <http://solarb.mssl.ucl.ac.uk:8080/eiswiki/>

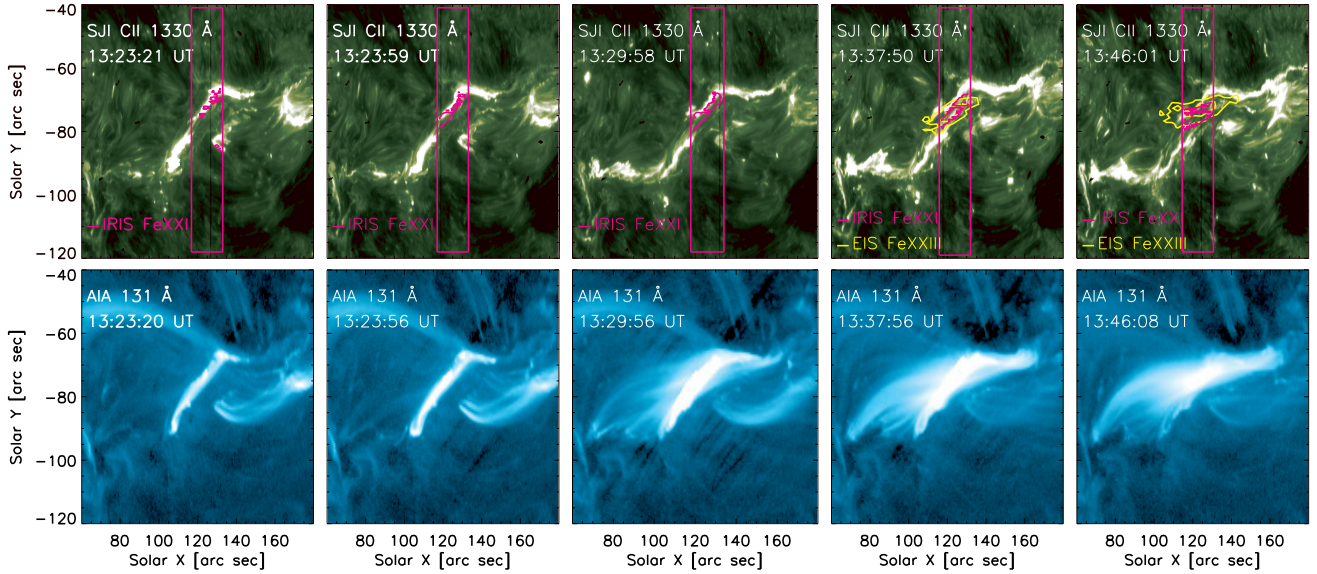


Figure 5. First row: IRIS SJI C II 1330 Å images with IRIS Fe XXI (pink) and EIS Fe XXIII (yellow) contours overplotted. The EIS observations start at about 13:35 UT. The pink box indicates the IRIS spectrograph field of view. Second row: AIA 131 Å corresponding closest images in time. During flares, the AIA 131 Å channel is dominated by Fe XXI emission, formed at $T \gtrsim 10$ MK.

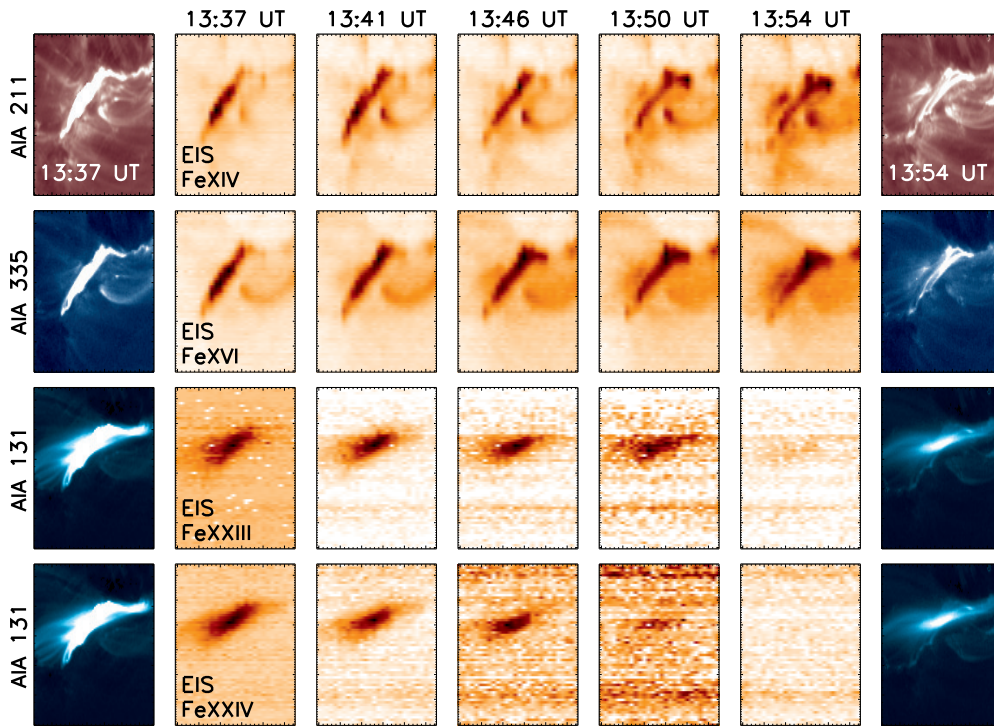


Figure 6. AIA and EIS images of the flare loops during the gradual phase, zoomed along the solar x coordinates 80 to 170 arcseconds and solar y coordinates -120 to -40 arcseconds in fig. 5. The central part of the multi-panel figure (column 2 to 6) show EIS monochromatic images (negative color table) obtained in different emission lines with increasing formation temperature from the top to the bottom. The timing of the EIS maps increase from left to right and is indicated on each EIS map on the first row. The first and last columns show AIA images at different temperatures closest to the formation temperature of the EIS emission line represented on the same row. They are co-temporal to the mid-point of the first and last EIS rasters respectively.

shifting towards the middle of the two ribbons but it still mainly originates from the northern ribbon. Finally, the fourth and the fifth SJI images show the flare during the gradual phase, when EIS was also observing the event. Figure 5 shows that during the rising phase of the flare the Fe XXI emission only originates from the ribbon, sug-

gesting that the high temperature emission was evaporating from the footpoints at the onset of the flare. Indeed, this early Fe XXI emission is found to be blue-shifted (see Sect.4). It is important to note that we do not observe Fe XXI emission along the loops top before the evaporation takes place.

As the flare loops are filled by hot temperature plasma evaporating from the ribbons, we see the Fe XXI and Fe XXIII intensities progressively moving towards the top of the loop structures (last two SJI images in fig.5). At the same time, there is no more appreciable hot plasma emission coming from the northern ribbon.

By observing the evolution of AIA 131 Å and spectroscopic images over time, we can also note that the morphology of the hot loops during the gradual phase change from the fourth ($\sim 13:37$ UT) to the fifth ($\sim 13:46$ UT) image. At about 13:37 UT, a set of hot loops connects the closest parts of the two ribbons. In the fifth image, the loops appear stretched and connect more distant locations along the ribbon.

In addition, the evolution of 2-3 MK as well as ~ 10 MK plasma is observed by EIS during the gradual phase of the flare. Figure 6 shows AIA images and EIS monochromatic images of the flare loops from about 13:35 to 13:56 UT. The central columns (from 2 to 6) present EIS negative intensity maps in different lines with increasing temperature of formation from the top to the bottom. The EIS monochromatic images were isolated by performing Gaussian fitting of each spectral line. The timing of the EIS maps increases from left to right and is indicated on each map (top). The first row shows the Fe XIV 264.78 Å emission, which is formed at ~ 2 MK. Fe XVI 262.98 Å intensity maps are reported in the second row; this line is formed at about 3 MK. Finally, the third and fourth rows show Fe XXIII 263.76 Å and Fe XXIV 255.11 Å, which are both formed at very high temperatures above 10-12 MK. Figures 6 and 5 show a similar plasma morphology in the EIS Fe XXIII, Fe XXIV and IRIS Fe XXI emission during the gradual phase.

Moreover, in figure 6 we compare the evolution of the monochromatic plasma observed by EIS with AIA images taken at the beginning and the end of the EIS maps sequence. For each emission line, we have chosen the AIA filter which is dominated by plasma formed at similar temperature. During flares, the dominant contribution to the 211 Å, 335 Å and 131 Å AIA bands comes from Fe XIV ($T \sim 2MK$) and Fe XVI ($T \sim 3MK$) and Fe XXIII-Fe XXIV ($T > 10MK$) lines respectively (O'Dwyer et al. 2010; Petkaki et al. 2012). We can therefore compare images in these AIA filters to the corresponding emission lines observed by EIS. The difference between the plasma formed at about 2-3 MK (Fe XIV/AIA 211 Å, Fe XVI/AIA 335 Å) and at higher temperatures (Fe XXIII and Fe XXIV/AIA 131 Å) suggests that cooler and hotter emissions originate from different loop structures along the line-of-sight. After $\sim 13:52$ UT we observe no appreciable emission in the Fe XXIII and Fe XXIV spectral lines.

4. IRIS Fe XXI OBSERVATION AND RESULTS

Fe XXI 1354.08 Å is the highest temperature emission line observed by IRIS. During solar flares, the intensity of this line is enhanced and becomes comparable to that of the chromospheric lines in the same spectral range. Sect. 4.1 describes the analysis of the O I 1356 Å spectral window, including the wavelength calibration procedure and a discussion about possible line blendings. The discussion about blue shifts and the line profile results are given

in sect. 4.2.

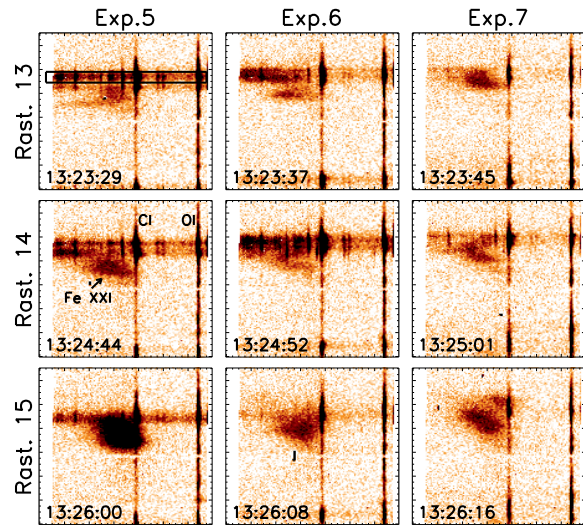


Figure 7. IRIS Spectrograph FUVS detector images of the O I 1356 spectral window. Blue asymmetries in the Fe XXI 1354.08 Å line profile are particularly visible from raster 13 to 15. They are more intense in the raster exposure no. 5, but occur also at locations where the slit was scanning the raster exposures no.6 and 7. To estimate possible blends with the Fe XXI line, a spectrum was acquired in the raster no.13, exposure 5 (black box), where many usually weak chromospheric lines are enhanced. The narrow O I 1355.60 Å and C I 1354.29 Å chromospheric lines and the broad Fe XXI 1354.08 Å line are indicated in the figure (raster 14, exp.5)

4.1. The IRIS O I 1356 Å spectral window

As a result of the temperature variation of the detectors and the change of the spacecraft-Sun distance, the wavelength scale of the IRIS detectors drifts by about 8 km s^{-1} (FUV channel) during one orbit. The orbital variation of the line positions can be corrected by using the routine *iris_orbitvar_corr_l2.pro*. The spacecraft velocity is the same for the FUV and NUV detectors and is subtracted from both the wavelength arrays, while the thermal component introduces an anti-correlated drift between the two channels. The *iris_orbitvar_corr_l2.pro* routine uses the strong NUV Ni I 2799.47 Å line (included in the IRIS line list by default) to correct both FUV and NUV spectra². The difference between the orbital corrections for the two bands are around 0.8 km s^{-1} . In order to test this method on our specific data set, we have plotted the centroid position of the uncorrected O I 1355.60 Å neutral line (included in the same window as Fe XXI) over time and found drifts which are consistent with the correction factors calculated by *iris_orbitvar_corr_l2.pro* routine.

When measuring velocity shifts in spectral lines, it is also necessary to perform an absolute calibration of the wavelength array. The doppler shift of the photospheric O I 1355.60 Å line is often less than 1 km s^{-1} and therefore represents a suitable reference line to perform an absolute spectral calibration. After applying the orbital correction, we verified that the O I centroid position does not drift over time and that it does not vary along the slit (within the $\sim 1 \text{ km s}^{-1}$ uncertainty). For each exposure,

the centroid position of the line has been averaged over a portion of the slit where the emission was stronger. Finally, the difference between this value and the expected rest wavelength 1355.598 Å (Sandlin et al. 1986) has been subtracted from the wavelength array.

During the gradual phase ($\sim 13:44$ UT, fig.11) we measure a centroid position of 1354.08 ± 0.01 Å for the Fe XXI spectral line, which we adopt as the rest wavelength in this study. The error has been obtained by adding the uncertainties associated to the Fe XXI and O I centroid positions as derived from the fit, and the accuracy of the O I 1355.60 Å rest wavelength (~ 1 km s^{-1} due to doppler shifts in the solar atmosphere). We note that the Fe XXI rest wavelength value is in good agreement with 1354.08 ± 0.05 Å from Sandlin et al. (1986). Within the error, our result is also consistent with the value of 1354.106 ± 0.023 Å which was recently found by Young et al. (2014).

In addition, it is important to consider possible blendings with the Fe XXI line. Figure 7 shows detector images (solar Y coordinates vs wavelength) of the FUVS O I spectral window corresponding to the exposures no. 5, 6 and 7 of raster no.13 to 15 (13:23:29-13:26:16 UT). These images are zoomed in the solar-Y direction (i.e. along the IRIS slit) from pixels 720 to 850. The two narrow emission lines visible along all the slit represent the C I 1354.29 Å and the O I 1355.60 Å emission (from left to right). The broad emission is in contrast coming from the hot Fe XXI 1354.08 Å line, partially blended with the C I 1354.29 Å. We can also note that the usually weak emission from many chromospheric lines is visibly enhanced in some locations along the slit which spatially overlap to the northern ribbon. Fig.8 shows a spectrum (black) of the IRIS O I 1356 window in one of these locations (raster 13, exposure 5), which is indicated by the black box in fig.7. The blue color represents the Gaussian fits of the line profiles.

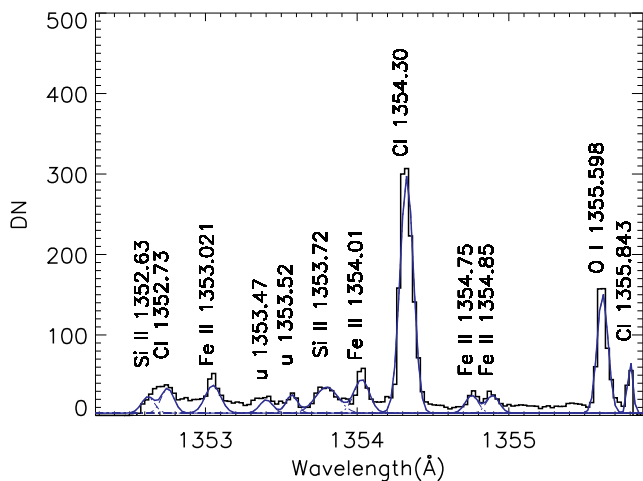


Figure 8. Spectrum (black) of the IRIS O I 1356 Å window acquired along the northern ribbon (black box in the detector images in fig.7, raster no.13 and exposure no.5). The spectral lines are fitted with Gaussian profiles (blue).

² <http://iris.lmsal.com/documents.html>

We identified some low temperature (chromospheric) lines whose intensity is typically less than $\sim 1/10$ the intensity of the O I 1355.60 Å line in a plage region (Sandlin et al. 1986; Cohen 1981). Considering that in all the spectra analysed in this work (see sect.4) the intensity of the O I 1355.60 Å line is always below ~ 50 counts, we can expect these cool lines to be there very weak. In addition, it is important to note that the emission from these lines is not particularly enhanced in the specific locations where we observe blue-shifts in the the Fe XXI profiles (see sect. 4.2). In contrast to what is found by Young et al. (2014) in an X1 class flare, we can conclude that the eventual blending with cool lines on the blue-side of the Fe XXI spectral line would not represent a major issue in our analysis.

C I 1354.29 Å is the only strong line which significantly blends with the Fe XXI on its red side. However, this line is narrow and easy to deblend especially when the Fe XXI profile is entirely blue-shifted. The position and width of the C I line do not change over time and they are found to be around ~ 1354.29 Å and 0.06 Å respectively. In order to reduce the uncertainty associated with the multi-component fit, we have fixed these parameters when deblending the C I from the Fe XXI line.

4.2. Fe XXI line profile

Blue shifts in the Fe XXI line profile are visible during the impulsive phase from about 13:23 UT (raster no.13), when the Fe XXI emission appears for the first time. They gradually decrease until 13:29:48 UT (raster no. 18). These blue shifts are better observed in the detector images which show the emission along the slit Y-direction as a function of wavelength for the different exposures contained in each IRIS raster (fig. 7). Similar features are observed in the exposures 5-6-7 in fig. 7, but we have selected the only exposure 5 to perform a more detailed spectral analysis. The slit exposure no. 5 corresponds in fact to the position along the ribbon where the blue shifts are first observed and where they are more intense.

By observing the IRIS SJI and AIA images, we also can spatially locate (in Solar-Y vs Solar-X coordinates) the regions where these blue shifts originate. Figure 9 shows AIA 131 Å and SJI 1400 Å images co-temporal to the slit exposure number 5 from raster no. 13 to 18. The slit position is indicated by the vertical double lines. Fe XXI 1354.08 Å profiles were acquired at these locations and are shown in fig.10. For each exposure, the spectrum has been spatially averaged over the slit Y-pixels where the line emission was most intense. In addition, the Y-pixels were carefully chosen in order to avoid any possible blending with cool emission lines visible in the upper part of the ribbon (see fig.7).

Some of the Fe XXI profiles in fig.10 (rasters 13, 14, 17, 18) are symmetric or almost symmetric and have been fitted with a single Gaussian component. Others (rasters 15, 16) present evident non-Gaussian profiles with an asymmetry on the blue side, which can be interpreted as the superposition of two plasma components. In this latter case, we have performed a double Gaussian fit: one rest component with centroid position at rest and fixed width, one blue shifted component with variable velocity and width. The fit parameters (centroid, FWHM and ve-

Table 2
Fe XXI fit parameters

Raster no.	Time UT	Wavelength (Å)	Velocity (km/s)	FWHM (Å)	W_{non-th} (km/s)
13	13:23:31	1353.71 ± 0.03	82.0±7.6	1.00±0.07	127.5±8.7
14	13:24:46	1353.78±0.03	66.4±5.5	0.83± 0.04	94.5±5.1
15	13:26:02	1353.93± 0.02	33.2±5.1	0.78±0.03	86.7±3.7
16	13:27:17	1353.87±0.04	46.4±8.1	0.76±0.03	83.5±4.7
17	13:28:33	1353.98±0.02	22.1±3.4	0.56±0.02	47.9±1.8
18	13:29:48	1354.01±0.01	15.5±2.4	0.55±0.01	45.8±1.1
30	13:44:55	1354.08±0.01	0	0.43±0.07	0

locity) are given on the top right of each subfigure in fig 10 and table 2. For profiles where a double-Gaussian fit has been performed (raster 15 and 16), the fit parameters refer to the blue variable component, while the rest component has fixed wavelength (1354.08 Å, indicated by the vertical blue line in each spectrum) and width (0.43 Å). The errors associated to these parameters are calculated by the linear sum of the errors of the Fe XXI and O I positions as derived from the fit, and the estimated 1 km s^{-1} uncertainty for the O I 1355.60 Å rest wavelength calibration.

The rest wavelength is the estimated centroid rest position (1354.08 ± 0.01 Å) after the wavelength calibration has been performed, as explained in sect.4.1. The width of the rest component (0.43 Å) is given by the quadratic sum of the IRIS instrumental FWHM (0.026 Å; De Pontieu et al. (2014)) and the line thermal width assuming temperature of $1.1 \cdot 10^7 K$ (peak temperature of the ion abundance as derived from CHIANTI v7.1 (Dere et al. 1997; Landi et al. 2013)). The rest wavelength and width so determined agree very well with the fit parameters of a profile acquired during the gradual phase at the hot temperature loops (fig.11), when we expect the line position to be at rest.

The observed blue-shifts and non-thermal velocities over time are plotted in fig.12. The non-thermal velocities W_{non-th} are given by

$$W_{non-th} = \sqrt{(4ln2)^{-1} \left(\frac{\lambda}{c}\right)^{-2} \cdot (W^2 - W_{th}^2 - W_I^2)} \quad (1)$$

where W is the line FWHM obtained from the fit, W_{th} is the thermal width, W_I is the IRIS instrumental FWHM, λ is 1354.08 Å and c is the speed of light. The non thermal widths (km s^{-1}) of the blue-shifted component are also given in table 2 for each spectrum in fig. 10. As shown in fig.10, in the early phase of the flare we see a totally blue shifted and very broad (more than twice than the thermal width) Fe XXI profile. During this phase, the Fe XXI intensity is coming entirely from the ribbon (fig. 5). We can therefore interpret the observed blue-shifts as being caused by evaporation from the flare footpoints, as mentioned in sect. 3. Going towards the peak of the flare, the velocity and non-thermal width of this emission then gradually decrease. At the same time, we see an increase of the rest emission that we can interpret this as coming from the hot loops as they fill, in agreement with a chromospheric evaporation scenario

in flares. A more detailed discussion will be given in sections 6.1 and 6.2.

5. EM AND DENSITIES FROM IRIS/EIS/AIA OBSERVATIONS

The intensity $I(\lambda)$ of an optically thin spectral line can be expressed as

$$I(\lambda) = \int_h N_e N_H A(X) G(N_e, T, \lambda) dh \quad (2)$$

where N_e and N_H are the electron and hydrogen number densities, $A(X)$ is the element abundance relative to hydrogen, the $G(N_e, T)$ is the contribution function of the line and the integral is performed along the line-of-sight h . The column emission measure (EM) is defined as

$$EM_h = \int_h N_e N_H dh \quad (3)$$

and so depends on the physical conditions of the emitting plasma along the line of sight h .

For an isothermal plasma at temperature T_0 , the emission measure of a spectral line can then be expressed as

$$EM_h(\lambda) = I_{obs}(\lambda) / (A(X)G(N_e, T_0)) \quad (4)$$

The loci of the curves $I_{obs}/G(N_e, T)$ at a given density N_e therefore provides an upper limit to the value of the emission measure at the equilibrium temperature T_0 (Del Zanna et al. 2002). In figure 14, we plot the ratio $I_{obs}(\lambda)/G(N_e, T)$ for the IRIS Fe XXI 1354.08 Å, EIS Fe XXIII 263.76 Å, Fe XXIV 255.11 Å and 192.03 Å spectral lines observed at the loop top at two different times during the gradual phase (\sim 13:38 and 13:42 UT) of the flare. The intensity $I(\lambda)$ of the EIS and IRIS lines has been averaged over the box indicated in figure 13 and converted from data number (DN) to physical units (erg $s^{-1} sr^{-1} cm^{-2} \text{Å}^{-1}$). The conversion of the EIS DN to intensity units is derived as described in the EIS Software note no.2¹, The radiometric calibration of the IRIS data is detailed in the IRIS software note no. 24². The factor $G(N_e, T_0)$ in eq. 4 is calculated by using the *gofnt.pro* routine available within the CHIANTI package (Dere et al. 1997; Landi et al. 2013), assuming photospheric abundances. Moreover, we can estimate the column emission measure from AIA observations in the 131 Å channel. During flares, this band is dominated by Fe XXI (Petkaki et al. 2012), which is formed at the same temperature (\gtrsim 10 MK) to the observed IRIS (Fe XXI) and a similar temperature to the EIS

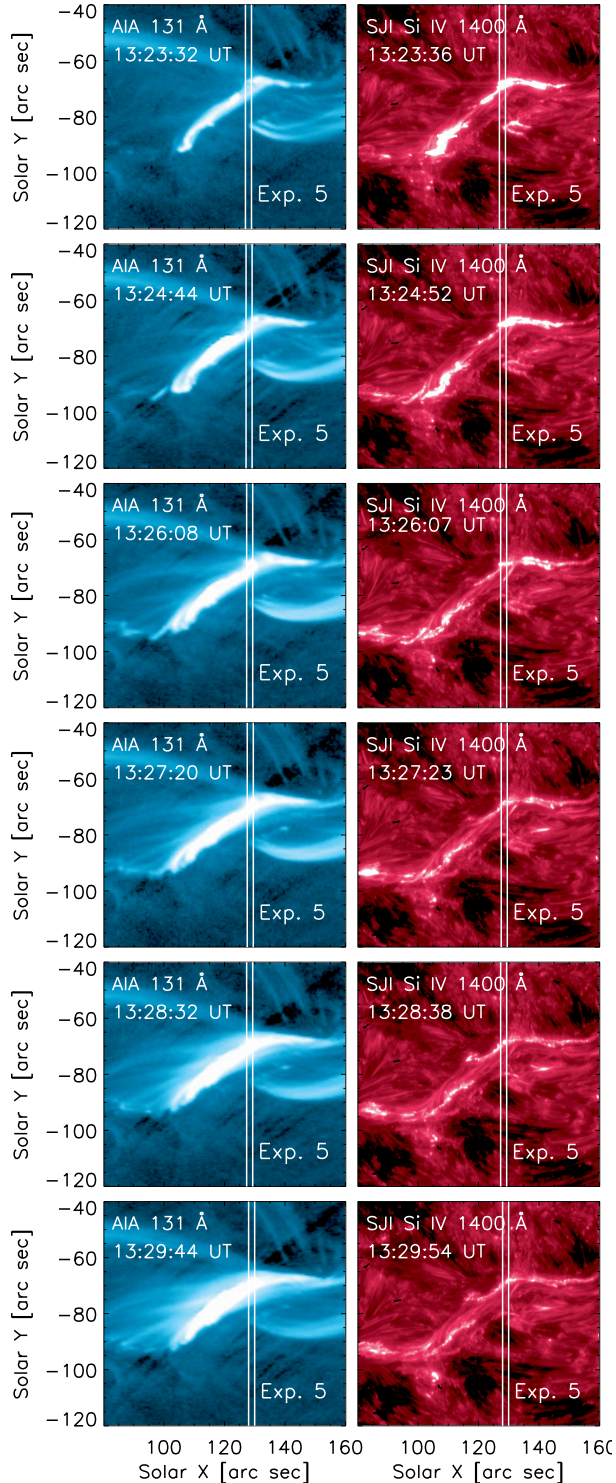


Figure 9. AIA 131 Å and IRIS SJI 1400 images at different times during the rising phase of the flare, from raster no.13 to no.18. The white vertical lines define the position of the IRIS spectrograph slit corresponding to the raster exposure no. 5

(Fe XXIII and Fe XXIV) lines. For AIA observations, the column emission measure can be expressed as

$$EM_h = I_{obs}(131 \text{ \AA})/R(N_e, T_0) \quad (5)$$

where $R(N_e, T_0)$ is the AIA 131 Å temperature response.

The response was calculated by using the AIA effective areas and new atomic data from CHIANTI v 7.1 as described in Del Zanna et al. (2011b). The count rates $I_{obs}(131 \text{ \AA})$ have been obtained by averaging the AIA 131 Å intensity maps over the same location shown in figure 13.

The curves in figure 14 consistently show an isothermal loop structure within an estimated 25 % error at a temperature of about 13.5 MK at around 13:38 UT (four minutes after the peak of the flare). By 13:42 UT, the loop top temperature has dropped to about 12 MK as shown in figure 14. The cooling of the flare loops is more evident in the hotter Fe XXIII and Fe XXIV lines rather than in the Fe XXI line, which is expected to be formed at somewhat lower temperatures. The main uncertainty associated to the EM_h curves is due to the error in the observed intensity and thus to the absolute calibration of IRIS, EIS and AIA. The radiometric calibration of the EIS spectrometer has been revised (Del Zanna 2013) to take into account the degradation of the optical components over time. In particular, by 2010 the efficiency of the long wavelength (LW) channel has been found to drop of a factor ~ 2 from the on-ground calibration value. For instance, Del Zanna (2013) estimates a Fe XXIV 192.03/255.11 ratio of about 1.5 after the launch. However, the emission measure curves obtained in this work from the two different Fe XXIV lines still differ of a factor of about 1.5. The EIS calibration by Warren et al. (2014) yields a Fe XXIV line ratio of about 2.5 and would therefore give a more consistent value to the theoretical ratio. Finally, it is important to note that both revised calibrations are based on observational results acquired until 2013; the EIS radiometric calibration might therefore need to be further revised by using some more recent observations.

The in-flight stellar calibration of the IRIS throughput (IRIS software note no. 24²), has shown an average 23 % decrease in the short FUV wavelength spectrograph channel compared to the pre-launch values. The IRIS team is currently investigating the changes in the instrument effective areas after launch. In the present work, we have used the pre-launch values obtained with the routine *iris_get_response*. It is interesting to note that a depression in the sensitivity of the FUVS spectrograph channel would provide higher values of emission measure derived from the Fe XXI line and therefore a better agreement between the EM curves shown in fig 14.

An uncertainty of ~ 25 % can be assumed for the photometric calibration of SDO/AIA (Boerner et al. 2012). Finally, the error bars in figures 14 indicate a 25 % uncertainty for the estimates of EM_h values.

5.1. Loop top density estimates

With some assumptions, the EM analysis also allows us to estimate a lower limit for the flare plasma density. Equation 3 can in fact be expressed as $EM_h \simeq 0.83(N_e)^2 \Delta h$ where Δh is the column depth of the emission layer and $N_H = 0.83N_e$ in a fully ionized gas with helium abundance relative to hydrogen $A(He) = 0.1$. In addition, we have assumed a *spectroscopic filling factor* equal to 1. The depth Δh can be estimated from the width of the loop structures visible in the AIA 131 Å images, assuming that the

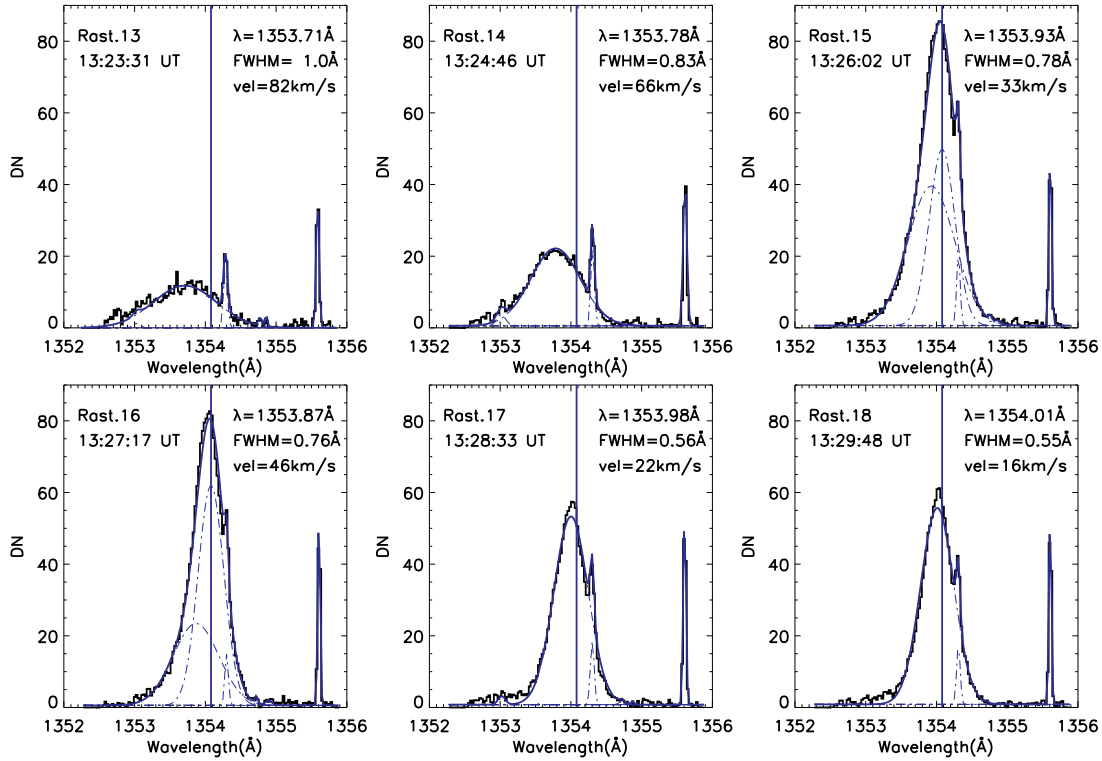


Figure 10. Fe XXI profiles during the rising phase of the flare, from about 13:23 UT to 13:29 UT. The corresponding slit position is shown on SJI and AIA images in figure 9. The vertical blue line represents the Fe XXI rest wavelength position. The fit parameters (wavelength, FWHM and velocity of the blue-shifted component) are reported in each spectrum.

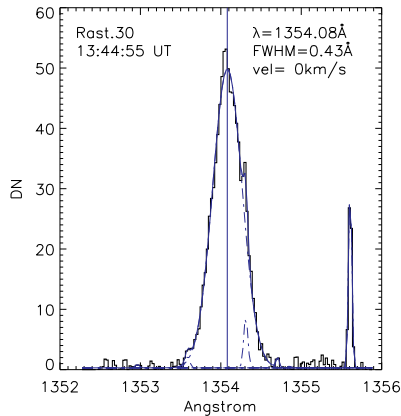


Figure 11. Fe XXI spectrum acquired during the gradual phase of the flare (13:44:55 UT) at the top of the loop. The profile fits the expected rest position and thermal width corresponding to a temperature of peak emission of $1.1 \cdot 10^7$ MK

loops are circular. We obtained widths of $\sim 3.7 \cdot 10^8$ cm corresponding to electron densities N_e at the top loop of $\sim 6.1 \cdot 10^{10} \text{ cm}^{-3}$ and $\sim 5.1 \cdot 10^{10} \text{ cm}^{-3}$ at two different times ($\sim 13:38$ UT and $13:42$ UT) during the gradual phase. It is important to point out that if one assumes "coronal" abundances (e.g. with Fe abundance increased by a factor 4 from the photospheric value, Feldman (1992)), the densities become smaller by a factor ~ 2 . In addition, these density values represent a lower limits due to the assumption of a filling factor equal to 1.

6. DISCUSSION AND SUMMARY

In this work we have presented the analysis of a joint IRIS/EIS observation of a small C6.5 class flare occurring on the Sun on the 3rd February 2014. Simultaneous IRIS Slit Jaw Imager (SJI) and the SDO/AIA images have been used to study the evolution of the hot flare plasma over time and to provide useful context information for our analysis.

The IRIS spectrograph provides instrumental capabilities to study upflows in the Fe XXI 1354.08 Å spectral line evaporating from the kernels during the early phase of the flare. For this particular flare, we feel confident that we are able to resolve the high temperature Fe XXI emission from the cool chromospheric lines present in the same spectral window.

Thanks to the high spatial and temporal cadence of IRIS, we were able to follow in great detail the evolution of Fe XXI over time.

6.1. Early blue shifted profiles

The first two Fe XXI profiles that we observe (13:23:31 UT and 13:24:36 UT respectively) are completely blue shifted, in agreement with the model prediction that a single blue-shifted component should be observed at the flare onset (Emslie & Alexander 1987). This is also consistent with previous observations in the

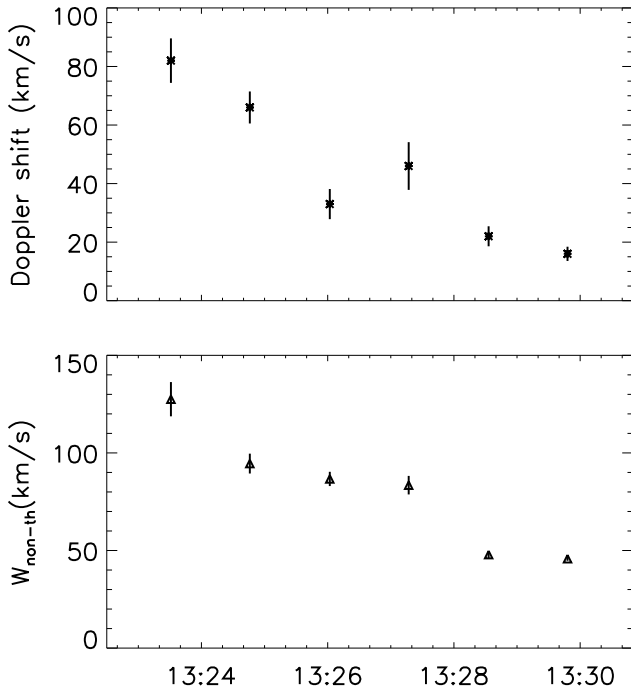


Figure 12. Fe XXI velocities and non-thermal widths during the rising phase of the flare, from about 13:23 UT to 13:29 UT. These parameters were obtained by single or double-Gaussian fit of the spectra shown in fig.10, as described in sect.4.2.

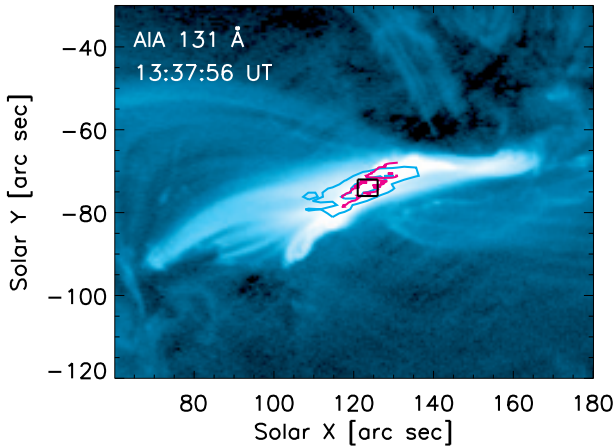


Figure 13. AIA 131 Å image of the top loop with the IRIS Fe XXI (pink) and EIS Fe XXIII (blue) intensity contours. The black box indicate the location where we have measured the plasma emission measure.

Fe XIX (formed at ~ 9 MK) with CDS (Del Zanna et al. 2006; Milligan et al. 2006) and in Fe XXIII-Fe XXIV lines ($T > 10$ -15 MK) observed by EIS (Watanabe et al. 2010; Del Zanna et al. 2011a; Brosius 2013a; Young et al. 2013). It is important to note that at the time when the Fe XXI evaporation first occurs, this emission only comes from the flare footpoints and no Fe XXI flare loops are yet observed.

The fact that an initial completely blue-shifted component has not been systematically observed in previous studies could be explained if the line intensities during

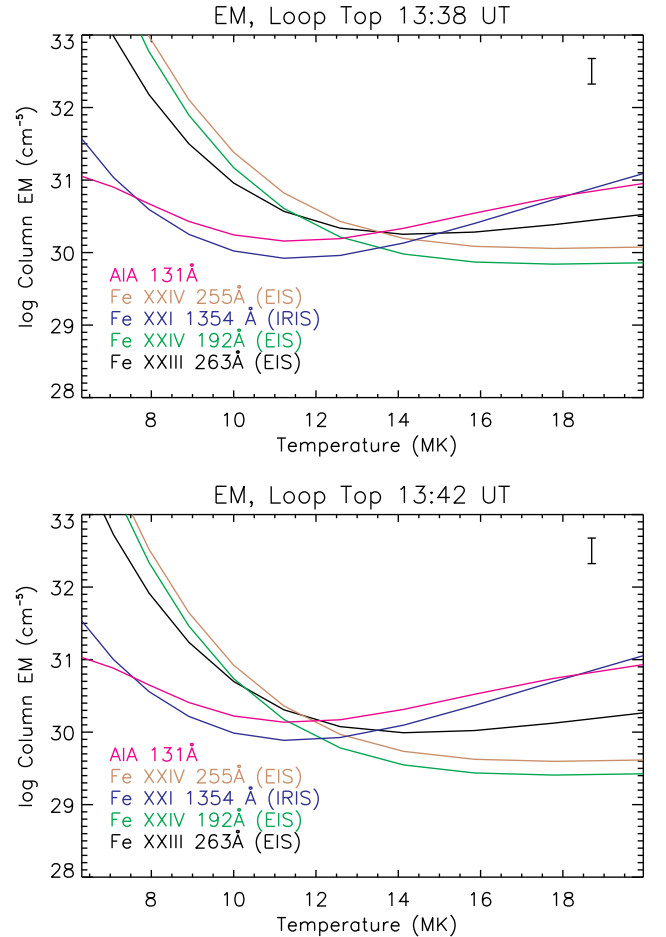


Figure 14. Emission measure plot from IRIS (Fe XXI 1354.08 Å) and EIS (Fe XXIII 263.76 Å, Fe XXIV 192.03 and 255.11 Å) spectral lines and AIA 131 Å observations at the loop top at two different times during the gradual phase ($\sim 13:38$ UT (top) and $\sim 13:42$ UT (bottom)). The error bar in each figure represents a 25% uncertainty for the estimates of EM values.

the impulsive phase are too weak and the blue shifts too rapid to be detected (Antonucci 1989). As clearly shown in fig. 10, it is in fact very easy to miss the early impulsive phase, where the line emission is completely shifted but very weak. Also, IRIS has a much better spatial resolution than every previous spectroscopic instrument, which may be another reason why we are able to observe a fully blueshifted line.

The first observed Fe XXI emission shows a very broad profile with an estimated centroid blue-shift velocity of $\sim 82.0 \pm 7.6$ km s^{-1} . This value is consistent with the average upflow velocity (~ 100 km s^{-1}) recently observed in the IRIS Fe XXI by Young et al. (2014) at the footpoints of an X1 class flare during the rising phase. However, these speeds are much smaller than the ones which have been sometimes observed in the hotter EIS Fe XXIII and Fe XXIV flare lines during the impulsive phase (Milligan & Dennis 2009; Watanabe et al. 2010; Young et al. 2013). This may partly be explained in terms of the predicted velocity trend with increasing temperature of line formation (Del Zanna et al. 2006). Another factor that it is certainly worth considering is the effect of the line-of sight on our velocity estimates. Considering that the loops might be

tilted compared to the observer direction, the measured speeds would clearly represent lower limits to the actual upflowing velocities along the loops.

In addition, we cannot rule out the presence of a component blue shifted by more than 350 km s^{-1} , which would not be observed within the IRIS spectral window; however, the high temporal cadence of the observed blue shifts suggests that this would be unlikely.

Since the evolution of the chromospheric evaporation during the impulsive phase is known to be very fast, higher cadence (better than 75 s) and better sensitivity observations would be needed to confirm that we are not still missing an earlier more blue-shifted and fainter evaporating emission.

6.2. Evolution of the blue shifts over time

From fig.12 we can observe that the velocity of the blue shifted component gradually decrease over time until the emission comes to a complete rest in about 6 minutes. This can be interpreted in terms of a decrease in the pressure difference along the flare loops (Antonucci 1989). The first two profiles observed in fig 10 (13:23:31-13:24:36 UT) are in fact totally blue shifted; from about 13:26:02 UT, while these blue shifts decrease, the rest emission becomes progressively more intense. We interpret the rest emission as originating from the overlying flare loops which are being filled with the evaporating Fe XXI plasma over the previous minutes. Some of the observed Fe XXI spectra are thus fitted by blue-asymmetric two-component profiles, each composed of a broad blue shifted and a thermal rest component, in contrast to what was found by Young et al. (2014) where only single shifted profiles were observed. By about 13:30 UT (~ 4 min prior to the peak of the flare), there is no more appreciable blue shifted emission and the profile is composed of only a single almost at rest and thermal component, suggesting that the evaporation in this particular site has already concluded.

Similar blueshifted profiles are also observed at other locations along the ribbon (raster exposures 6 and 7, see fig. 7) with a slight time delay. One possible interpretation is that the evaporation takes place at progressively more distant locations along the flare ribbons. In addition, at later times the inclination of the hot loop structures observed in AIA 131 Å images gradually decrease compared to the orientation of the ribbons. This evidence might suggest that a magnetic “slipping” reconnection (Dudík et al. 2014) was taking place.

6.3. Non thermal widths

Very broad non-thermal widths (up to $\sim 127 \text{ km s}^{-1}$) are observed during the impulsive phase of the flare from about 13:23:31 UT to 13:27:17 UT. During the observations the Fe XXI profile is in contrast observed to be thermal at the loop tops, i.e. the line width there is consistent with the expected width at the temperature of the Fe XXI peak abundance in equilibrium ($\sim 11 \text{ MK}$), in agreement with early results by Mason et al. (1986) and more recently by Young et al. (2014). Both the non-thermal width and the velocity of the blue shifted component are observed to gradually decrease, as shown in fig.12. While blue-shifts of line profiles have already been

observed to decrease with time, to our knowledge this is the first time that non-thermal widths at the flare foot-points are observed to progressively decrease in the same specific location and with such a high temporal resolution ($\sim 75 \text{ s}$ cadence).

In addition, we would like to point out that the non-thermal excess that we observe is significantly different from the width enhancements analyzed in early observations of soft X-ray asymmetric profiles (Antonucci 1989; Doschek 1990) during the impulsive phase. First of all, in these early studies it was not possible to spectrally resolve a two-component profile and therefore the non-thermal widths were measured including both the up-flowing and rest components. Moreover, the non thermal excess was observed to increase before the onset of the chromospheric evaporation and may not therefore have been related to the evaporating upflows. These broadenings were instead interpreted as due to turbulent and random mass motions, and were correlated with the appearance of hard X-rays sources preceding the main burst and the evaporation. Due to the lack of spatial resolution, it was also difficult to interpret these early results in terms of the standard flare models.

In our case, we do not observe any Fe XXI emission along the flare loops prior to the chromospheric evaporation taking place and the non thermal broadenings are instead significantly correlated with the evaporation velocities, as shown in fig.12. The fact that non-thermal excess of the line profiles is observed at the flare foot-points and not at the loop tops (neither in the impulsive nor in the gradual phase), suggests that they are unlikely to be caused by isotropic plasma motion due for example to extra heating processes taking place at the loop tops (e.g. magnetic reconnection).

In contrast, this is an indication that the physical process responsible for the line profile broadening is probably occurring at chromospheric heights, i.e. in the same place where the evaporation occurs. This excess broadening may be interpreted as a super-position of sub-resolution plasma flows at different velocities, caused for example by an isotropic spreading out of heated plasma at chromospheric footpoints or by a rapid sequence of evaporation flows in new continuously reconnected field lines, or both. In the second case, the fact that the two early broad profiles in fig.10 appear symmetric would require the velocities of the upflows to be randomly-distributed around the bulk velocity during a 8-seconds observation. The physical mechanism causing the heating of different loops should therefore occur in a very short timescale, i.e., orders of few seconds or less. Slipping magnetic reconnection motions up to 130 km s^{-1} have been observed by Dudík et al. (2014) and would possibly account for such a rapid mechanism.

Another possible and natural explanation for the line enhancements might be a rapid increase of the ion temperature of the Fe XXI at the sites where the evaporation occurs, caused by energetic electrons and protons penetrating into the chromosphere. Interpreting the non-thermal broadenings in terms of a temperature enhancement, would then result in effective ion temperatures of the order 60 to 40 MK for the broad Fe XXI profiles shown in the first two panels in fig 10 .

Within the present study, it is not possible to discern among different mechanisms responsible for the observed

line broadenings. We are investigating this issue with further observations and modelling, to attempt an interpretation of their physical origin.

6.4. Hot plasma at the loop top

At the very onset of the flare ($\sim 13:22$ UT) there is no appreciable Fe XXI emission at the loop top visible in the IRIS detector images. Fe XXI emission is in fact first seen at the loop top only after the evaporation has started. Later on, the Fe XXI emission is observed to gradually move southwards to the the top of the loops connecting the two ribbons (see fig.5), in further agreement with the scenario of chromospheric evaporation of hot plasma filling the flare loops. Finally, during the gradual phase, the Fe XXI emission is also co-spatial with the EIS high temperature Fe XXIII and Fe XXIV emission at the loop top (see fig.5). Co-temporal and co-spatial EIS, IRIS and AIA images have been used to derive emission measure information during the gradual phase of the flare. We consistently found isothermal structures at ~ 14 MK at $\sim 13:38$ UT, which then cool down to ~ 12 MK in about 4 minutes. These temperatures and an estimated lower limit on the electron density of about $5 - 6 \cdot 10^{10} \text{ cm}^{-3}$ are consistent with what has been found in similar small flares (Del Zanna et al. 2011a).

The IRIS instrument provides us with the unique opportunity to observe the Fe XXI 1354.08 Å flare line with unprecedented temporal and spatial resolution. In particular, co-temporal and co-spatial SJI images allow a comparison of the Fe XXI intensity and the low atmosphere emission in addition to an accurate method of spatially co-aligning IRIS/EIS and SDO. Future coordinated observations between IRIS, EIS and AIA (and also an X-ray spectrometer) are extremely important for providing a comprehensive analysis of chromospheric evaporation signatures and their possible interpretation in terms of solar flare models.

IRIS is a NASA small explorer mission developed and operated by LMSAL with mission operations executed at NASA Ames Research center and major contributions to downlink communications funded by the Norwegian Space Center (NSC, Norway) through an ESA PRODEX contract. Hinode is a Japanese mission developed and launched by ISAS/JAXA, with NAOJ as domestic partner and NASA and STFC (UK) as international partners. It is operated by these agencies in co-operation with ESA and NSC (Norway). AIA data are courtesy of NASA/SDO and the respective science teams. CHIANTI is a collaborative project involving researchers at the universities of Cambridge (UK), George Mason and Michigan (USA).

VP acknowledge support from the Isaac Newton Studentship, the Cambridge Trust, and the IRIS team at Harvard-Smithsonian Centre for Astrophysics. HEM and GDZ acknowledge support from the STFC. LG and KR are supported by contract 8100002705 from Lockheed-

Martin to SAO.

REFERENCES

- Antonucci, E. 1989, *Sol. Phys.*, 121, 31
 Antonucci, E., Gabriel, A. H., Acton, L. W., et al. 1982, *Sol. Phys.*, 78, 107
 Benz, A. O. 2008, *Living Reviews in Solar Physics*, 5, 1
 Boerner, P., Edwards, C., Lemen, J., et al. 2012, *Sol. Phys.*, 275, 41
 Brosius, J. W. 2003, *ApJ*, 586, 1417
 —. 2013a, *ApJ*, 762, 133
 —. 2013b, *ApJ*, 777, 135
 Brosius, J. W., & Holman, G. D. 2009, *ApJ*, 692, 492
 Carmichael, H. 1964, *NASA Special Publication*, 50, 451
 Cohen, L. 1981, *NASA Reference Publication*, 1069
 Culhane, J. L., Harra, L. K., James, A. M., et al. 2007, *Sol. Phys.*, 243, 19
 De Pontieu, B., Title, A. M., Lemen, J. R., et al. 2014, *Sol. Phys.*, 289, 2733
 Del Zanna, G. 2013, *A&A*, 555, A47
 Del Zanna, G., Berlicki, A., Schmieder, B., & Mason, H. E. 2006, *Sol. Phys.*, 234, 95
 Del Zanna, G., Chidichimo, M. C., & Mason, H. E. 2005, *A&A*, 432, 1137
 Del Zanna, G., Landini, M., & Mason, H. E. 2002, *A&A*, 385, 968
 Del Zanna, G., Mitra-Kraev, U., Bradshaw, S. J., Mason, H. E., & Asai, A. 2011a, *A&A*, 526, A1
 Del Zanna, G., O'Dwyer, B., & Mason, H. E. 2011b, *A&A*, 535, A46
 Dere, K. P., Landi, E., Mason, H. E., Monsignori Fossi, B. C., & Young, P. R. 1997, *A&AS*, 125, 149
 Doschek, G. A. 1990, *ApJS*, 73, 117
 Doschek, G. A., Dere, K. P., Sandlin, G. D., et al. 1975, *ApJ*, 196, L83
 Doschek, G. A., Kreplin, R. W., & Feldman, U. 1979, *ApJ*, 233, L157
 Doschek, G. A., & Warren, H. P. 2005, *ApJ*, 629, 1150
 Dudík, J., Janvier, M., Aulanier, G., et al. 2014, *ApJ*, 784, 144
 Emslie, G. A., & Alexander, D. 1987, *Sol. Phys.*, 110, 295
 Feldman, U. 1992, *Phys. Scr*, 46, 202
 Fletcher, L., & Hudson, H. S. 2008, *ApJ*, 675, 1645
 Fletcher, L., Dennis, B. R., Hudson, H. S., et al. 2011, *Space Sci. Rev.*, 159, 19
 Harrison, R. A., Sawyer, E. C., Carter, M. K., et al. 1995, *Sol. Phys.*, 162, 233
 Hirayama, T. 1974, *Sol. Phys.*, 34, 323
 Kamio, S., Hara, H., Watanabe, T., Fredvik, T., & Hansteen, V. H. 2010, *Sol. Phys.*, 266, 209
 Kopp, R. A., & Pneuman, G. W. 1976, *Sol. Phys.*, 50, 85
 Landi, E., Young, P. R., Dere, K. P., Del Zanna, G., & Mason, H. E. 2013, *ApJ*, 763, 86
 Lemen, J. R., Title, A. M., Akin, D. J., et al. 2012, *Sol. Phys.*, 275, 17
 Mason, H. E., Shine, R. A., Gurman, J. B., & Harrison, R. A. 1986, *ApJ*, 309, 435
 Milligan, R. O., & Dennis, B. R. 2009, *ApJ*, 699, 968
 Milligan, R. O., Gallagher, P. T., Mathioudakis, M., et al. 2006, *ApJ*, 638, L117
 O'Dwyer, B., Del Zanna, G., Mason, H. E., Weber, M. A., & Tripathi, D. 2010, *A&A*, 521, A21
 Petkaki, P., Del Zanna, G., Mason, H. E., & Bradshaw, S. J. 2012, *A&A*, 547, A25
 Sandlin, G. D., Bartoe, J.-D. F., Brueckner, G. E., Tousey, R., & Vanhoosier, M. E. 1986, *ApJS*, 61, 801
 Sturrock, P. A. 1968, *The Astronomical Journal Supplement*, 73, 78
 Warren, H. P., Ugarte-Urra, I., & Landi, E. 2014, *ApJS*, 213, 11
 Watanabe, T., Hara, H., Sterling, A. C., & Harra, L. K. 2010, *ApJ*, 719, 213
 Young, P., Tian, H., & Jaeggli, S. 2014, *ArXiv e-prints*
 Young, P. R., Doschek, G. A., Warren, H. P., & Hara, H. 2013, *ApJ*, 766, 127
 Young, P. R., O'Dwyer, B., & Mason, H. E. 2012, *ApJ*, 744, 14
 Young, P. R., Del Zanna, G., Mason, H. E., et al. 2007, *PASJ*, 59, 857